

# Accretion of low angular momentum material onto black holes: 2D hydrodynamical inviscid case.

Daniel Proga and Mitchell C. Begelman<sup>1</sup>

JILA, University of Colorado, Boulder, CO 80309-0440, USA; proga@colorado.edu,  
mitch@jila.colorado.edu

<sup>1</sup> also Department of Astrophysical and Planetary Sciences, University of Colorado at Boulder

## ABSTRACT

We report on the first phase of our study of slightly rotating accretion flows onto black holes. We consider inviscid accretion flows with a spherically symmetric density distribution at the outer boundary, but with spherical symmetry broken by the introduction of a small, latitude-dependent angular momentum. We study accretion flows by means of numerical 2D, axisymmetric, hydrodynamical simulations. Our main result is that the properties of the accretion flow do not depend as much on the outer boundary conditions (i.e., the amount as well as distribution of the angular momentum) as on the geometry of the non-accreting matter. The material that has too much angular momentum to be accreted forms a thick torus near the equator. Consequently, the geometry of the polar region, where material is accreted (the funnel), and the mass accretion rate through it are constrained by the size and shape of the torus. Our results show one way in which the mass accretion rate of slightly rotating gas can be significantly reduced compared to the accretion of non-rotating gas (i.e., the Bondi rate), and set the stage for calculations that will take into account the transport of angular momentum and energy.

*Subject headings:* accretion – hydrodynamics – black hole physics – outflows – galaxies: active – methods: numerical

## 1. Introduction

Some of the most dramatic phenomena of astrophysics, such as quasars and powerful radio galaxies, are most likely powered by accretion onto supermassive black holes (SMBHs). Nevertheless, SMBHs appear to spend most of their time in a remarkably quiescent state. SMBHs are embedded in the relatively dense environments of galactic nuclei, and it is natural to suppose that the gravity due to an SMBH will draw in matter at high rates, leading to a high system luminosity. However, this simple prediction often fails as many systems are much dimmer than one would expect.

To illustrate a key problem in constructing theoretical models for accretion onto a black hole, let us express the luminosity due to accretion as

$$L = \eta c^2 \dot{M}_a, \quad (1)$$

where we invoke the simplest assumption, that the luminosity is proportional to the mass accretion rate,  $\dot{M}_a$ , and an efficiency factor,  $\eta$ . The accretion luminosity is very uncertain because  $\eta$  is uncertain:  $\eta$  ranges from  $\sim 10^{-1}$  in a standard, radiatively efficient thin disk, to  $\sim 10^{-11}$  for spherically symmetric accretion from a low density medium (e.g., Shakura & Sunyaev 1973; Shapiro 1973; Mészáros 1975). The mass accretion rate is also a source of uncertainty in estimates of the accretion luminosity because  $\dot{M}_a$  depends on the physical conditions and geometry at large distances from the black hole. Nevertheless, it is customary to adopt the analytic formula due to Bondi (1952) to estimate the mass accretion rate. In his classic paper, Bondi (1952) considered spherically symmetric accretion from a non-rotating polytropic gas with uniform density  $\rho_\infty$  and sound speed  $c_\infty$  at infinity. Under these assumptions, a steady state solution to the equations of mass and momentum conservation exists with a mass accretion rate of

$$\dot{M}_B = \lambda 4\pi R_B^2 \rho_\infty c_\infty, \quad (2)$$

where  $\lambda$  is a dimensionless parameter that, for the Newtonian potential, depends only on the adiabatic index. The Bondi radius,  $R_B$ , is defined as

$$R_B = \frac{GM}{c_\infty^2}, \quad (3)$$

where  $G$  is the gravitational constant and  $M$  is the mass of the accretor.

The Bondi accretion formula predicts that SMBHs in typical galaxies should be more luminous than observations indicate when  $\eta$  is assumed to be as large as in a standard, radiatively efficient thin disk (e.g., Di Matteo et al. 1999, 2000, 2001; Loewenstein et al.

2001; Baganoff et al. 2001). In the context of equation (1), one possible explanation for this disagreement is that the black hole accretion flow can be radiatively inefficient because binding energy dissipated in the gas is advected through the event horizon before being radiated (Ichimaru 1977; Rees et al. 1982; Narayan & Yi 1994, 1995; Abramowicz et al. 1995). However, pure advection-dominated inflow may not be the whole story. Even before recent observations forced us to confront very low SMBH luminosities, theorists had begun to realize that rotating, radiatively inefficient hydrodynamical (HD) flows are subject to strong convection (Begelman & Meier 1982; Narayan & Yi 1995), which can fundamentally change the flow pattern and its radiative properties (Blandford & Begelman 1999; Quataert & Narayan 1999; Narayan, Igumenshchev & Abramowicz 2000; Quataert & Gruzinov 2000). The theoretical studies showed that convection alters the steep ( $\propto r^{-3/2}$ ) density profiles of the advection-dominated flow into a much flatter ( $\propto r^{-1/2}$ ) profile, which can explain the faintness of many SMBHs because it predicts relatively low density close to the black hole (i.e.,  $\dot{M}_a$  is low in eq. 2). Similar structural changes occur in the magnetohydrodynamical (MHD) limit (Stone & Pringle 2001; Hawley, Balbus, & Stone 2001; Machida, Matsumoto & Mineshige 2001; Igumenshchev & Narayan 2002; Hawley & Balbus 2002), although here the turbulence is probably driven by magnetorotational instability (MRI) rather than thermal convection (Balbus & Hawley 2002; but see Abramowicz et al. 2002 and Narayan et al. 2002 for alternative views).

The turbulent character of both HD and MHD models does not settle the issue of what happens to the energy and angular momentum that must be transported away. There are two possibilities: (i) turbulent transport effectively shuts off the accretion flow, turning it into a closed circulation (Narayan et al. 2000; Quataert & Gruzinov 2000) or (ii) turbulent transport drives powerful outflows that can strongly modify the black hole’s environment (Narayan & Yi 1994, 1995; Blandford & Begelman 1999). Recent MHD simulations bring new insights that may help us to resolve this issue. For example, Hawley & Balbus’s (2002) three-dimensional MHD simulations show that, with and without resistive heating, mass and energy in nonradiative accretion flows are carried off by an outflow in keeping with the outline of the second possibility.

Another possible solution to the problem of very low SMBH luminosity is that mass is captured into the accretion flow at a rate that is far lower than  $\dot{M}_B$ . Thus, a complete formulation of the accretion flow must also consider the outer boundary conditions. SMBHs draw matter from an extended medium and most authors assume that the Bondi (1952) formula provides an adequate approximation for the rate of mass supply. There has been little systematic work done to demonstrate that this assumption is justified and correct. Igumenshchev & Narayan (2002) showed that even non-rotating Bondi accretion can be altered, in particular that the mass accretion rate can be reduced below the Bondi rate. The

cause of the  $\dot{M}_a$  reduction in Igumenshchev & Narayan’s simulations is the local generation of energy through by magnetic reconnection, which leads to the development of efficient convection. However, in Igumenshchev & Narayan’s simulations the flow was supersonically injected into the computational grid through the outer boundary, at a specified rate (determined from the Bondi formula). Their calculations did not address self-consistently the problem of the mass accretion and supply rate because the latter was fixed at the outer boundary. As we mention above, the Bondi formula has been derived under the assumption that the gas is non-rotating and only under the influence of the central gravity. Thus, for a given gravitational field, the gas internal energy determines the accretion rate. By relaxing this assumption, introducing additional forces or sources of energy, one may find that the mass supply rate is much lower than the one predicted by the Bondi formula. For example, the rate at which matter is captured by a black hole can be severely limited when the matter is heated by X-rays produced near the black hole (Ostriker et al. 1976) or by mass outflow from the central region (Di Matteo et al. 2002). In these two cases, the gas internal energy is increased. Introducing kinetic energy to the gas at infinity may have a similar effect: although the flow outside the Bondi accretion radius often can be described as nonrotating, even a tiny amount of angular momentum,  $l$  — when followed inward — could severely limit the rate at which matter is captured by the black hole.

Our focus shall be on assessing the gross properties of rotating accretion flows onto black holes. We consider a classic Bondi accretion flow with the only modifications being the introduction of a small, latitude-dependent angular momentum at infinity and a pseudo-Newtonian gravitational potential. The imposed angular momentum is small enough to have a negligible effect on the density distribution at the outer boundary, which remains spherically symmetric. Therefore, matter near the rotational axis can be accreted. We thus consider a very simple model of an accretion flow, far simpler than those occurring in nature, as we neglect the gravitational field due to the host galaxy, radiative heating and cooling, viscosity and MHD effects. For example, we will not consider here the transport of energy and angular momentum outward, as needed to accrete matter with a specific angular momentum higher than  $2R_S c$  (where  $R_S = 2GM/c^2$  is the radius of a Schwarzschild black hole). Nevertheless, the results presented here provide a useful exploratory study of accretion onto black holes. In particular, our results constitute a “baseline” for evaluating the effects of dissipative and transport processes in subsequent work. They also serve as a “proof-of-concept” for the reduction of the mass accretion rate due to a small angular momentum in the accretion flow.

## 1.1. Expectations

Before we embark on a detailed analysis and numerical HD simulations, we first consider the problem of accretion of low- $l$  material in a general way. If the matter far from the SMBH (well outside the Bondi radius) has a uniform density and a specific angular momentum,  $l$ , which exceeds  $2R_S c$  — a tiny value compared to the Keplerian angular momentum at  $R_B$  — then no accretion will take place without angular momentum transport. After a transient episode of infall, the gas will pile up outside the black hole and settle into a nearly steady state atmosphere bounded by a centrifugal barrier near the rotation axis. Realistically, matter far from the SMBH will have a range of angular momenta, and in a steady state with axisymmetry, there will always be low- $l$  material close to the axis that can accrete steadily through a funnel along the rotational axis.

For this highly idealized problem, one would expect that the mass accretion rate should scale with the dependence of the angular momentum on the polar angle,  $\theta$ , at the outer radius,  $r_o$ : the larger the amount of the material with  $l > 2R_S c$  at  $r_o$ , the lower the mass accretion rate. This geometrical argument on the nature of the  $\dot{M}_a$  vs.  $l$  relation can be quantified as follows. If the angular momentum depends on  $\theta$  as

$$l(\theta) = l_0 f(\theta), \quad (4)$$

where  $f = 1$  on the equator ( $\theta = 90^\circ$ ) and monotonically decreases to zero at the poles ( $\theta = 0^\circ$  and  $180^\circ$ ), then a naive expectation would be that  $\dot{M}_a/\dot{M}_B$  scales with the solid angle within which  $l < 2R_S c$ :

$$\frac{\dot{M}_a}{\dot{M}_B} = \frac{\Delta\Omega_o}{4\pi} = 1 - \cos\theta_o, \quad (5)$$

where  $\theta_o$  is the width of the angular distribution for which  $l \leq 2R_S c$ . The latter can be formally defined as

$$\theta_o \equiv f^{-1} \left[ \min \left( 1, \frac{2R_S c}{l_0} \right) \right], \quad (6)$$

where  $f^{-1}$  represents the functional inverse of  $f$ . This simple geometrical argument is based on the assumption of radial flow and implies that if  $l \leq 2R_S c$  the material will be accreted approximately at the Bondi rate. If relation (6) were true then the accretion rate should decrease with increasing  $l_0$  for a fixed  $R_S$ . Additionally, one would expect that  $\dot{M}_a/\dot{M}_B$  should be independent of  $R_B$  for fixed  $R_S$  and  $l_0$ . However, to determine the actual mass accretion rate even in this idealized case we need to perform numerical simulations, as just HD effects of the inviscid fluid make the above geometrical argument invalid both quantitatively and qualitatively.

The main result of our numerical HD calculations is that the properties of the accretion flow do not depend as much on the outer boundary conditions (i.e., the amount as well as

distribution of the angular momentum) as on the geometry of the *non-accreting matter*. Material with  $l \gtrsim 2R_{Sc}$  cannot accrete and forms a thick torus near the equator. This thick torus and its formation have been a subject of numerous studies (see below). Our simulations show that the dependence of angular momentum on  $\theta$  in the torus gets weaker with decreasing radius. The material with  $l \gtrsim 2R_{Sc}$  inflows in the polar region, turns around as it reaches a centrifugal barrier, and then starts to outflow along the equator. As a result, a thick torus of nearly uniform specific angular momentum forms as gas of the highest angular momentum ( $l \approx l_0 > 2R_{Sc}$ ) near the equator is replaced by gas of lower angular momentum ( $l \gtrsim 2R_{Sc}$ ). The geometry of the polar region, where material is accreted (the funnel) and the mass accretion rate through it are constrained by the size and shape of the torus. We describe the size of the torus by an angle,  $\theta_t$ , between the torus's upper envelope and the pole at a characteristic radius.

Our HD models show that the  $\dot{M}_a$  vs.  $l$  relation has three regimes for a given  $f(\theta)$ : (i) for low  $l$  (i.e.,  $l < 2R_{Sc}$  for all  $\theta$  at large radii), the torus does not form and  $\dot{M}_a = \dot{M}_B$ , (ii) for intermediate  $l$ , or more appropriately where there is a narrow range of  $\theta$  for which  $l > 2R_{Sc}$  so  $\theta_o > \theta_t$ ,  $\dot{M}_a \sim \text{const}$  with the actual value of the constant depending on the ratio  $R_S/R_B$  and (iii) for high  $l$ , or in the case for which  $l > 2R_{Sc}$  at nearly all  $\theta$  so  $\theta_o < \theta_t$ ,  $\dot{M}_a$  decreases with increasing  $l_0$ .

Comparing the  $\dot{M}_a$  vs.  $l$  relation based on our HD models with that described by equation (5), we find that the two relations agree exactly in the first regime, disagree qualitatively and quantitatively in the second regime [the HD models predict  $\dot{M}_a$  lower than eq. (5)], and agree again but only qualitatively in the third region [the HD models predict  $\dot{M}_a$  higher than eq. (5)]. Thus the geometrical argument used above does not hold. However, we can use a modified version to describe the key aspects of the  $\dot{M}_a$  vs.  $l$  relation. The modification to the geometrical argument is to replace the solid angle within which  $l < 2R_{Sc}$  at the outer boundary,  $\Delta\Omega_o$ , with the solid angle within which  $l < 2R_{Sc}$  at a *characteristic radius comparable with the sonic radius*,  $\Delta\Omega_f$  (i.e., the solid angle of the accretion funnel). Thus,  $\dot{M}_a/\dot{M}_B \approx \Delta\Omega_f/4\pi$ . The insensitivity of  $\dot{M}_a$  to the angular momentum at infinity, in the second regime, can be attributed to the relative insensitivity of the torus, and thus the funnel, to the angular momentum distribution at infinity. In terms of the solid angle within which  $l < 2R_{Sc}$ , this corresponds to  $\Delta\Omega_f = \text{constant}$  for variable  $l_0$ , provided that  $\Delta\Omega_f < \Delta\Omega_o$  (i.e.,  $\theta_o > \theta_t$ ). On the other hand, the decrease of  $\dot{M}_a$  with increasing  $l_0$ , in the third regime, can be attributed to the fact that  $\Delta\Omega_f$  decreases with increasing  $l_0$ , provided that  $\Delta\Omega_f > \Delta\Omega_o$  ( $\theta_o < \theta_t$ ). We find that the mass accretion rate decreases with increasing  $l_0$  more slowly than predicted by eq. (5) in the third regime because the sonic point radius starts to increase as the funnel gets narrower.

## 1.2. Previous Work

Similar calculations have been performed before. For example, the formation of rotationally supported thick tori from inviscid accretion of gas with various initial angular momentum distributions has been reported (Hawley, Smarr & Wilson 1984a; 1984b; Clarke, Karpik & Henriksen 1985; Hawley 1986; Molteni, Lanzafame & Chakrabarti 1994; Ryu et al. 1995; Chen et al. 1997). However, there is one key difference between our work and some past work: our outer radial boundary is located outside the Bondi radius and we adopt subsonic, Bondi-like outer radial conditions whereas Molteni et al. 1994, Ryu et al. 1995, and Chen et al. 1997 (see also Toropin et al. 1999; Kryukov et al. 2000; and Igumenshchev & Narayan 2002) imposed outer boundary conditions inside the Bondi radius or even inside the sonic radius. The latter approach allows one to study cases where  $R_S/R_B$  is as low as in some real systems (e.g.,  $R_S/R_B = 10^{-5}$  in Chen et al. 1997) but this approach is not suitable for addressing our main issue: what is the mass supply rate. The approach adopted by Hawley et al. (1984a, 1984b), Clarke et al. (1985) and Hawley (1986) is much closer to ours as they also used subsonic outer boundary conditions. However, these authors did not consider how the accretion rate onto the black hole depends on the angular momentum distribution beyond the Bondi radius but rather focused on the formation of the thick torus. As far as the treatment of the outer radial boundary is concerned, our simulations are also similar for those of Ruffert (1994), who studied three-dimensional hydrodynamic Bondi-Hoyle accretion.

Other studies are also relevant to our work. Several authors considered accretion onto black holes with a focus on the evolution of rotationally supported thick tori including the transport of angular momentum and energy (e.g., Igumenshchev & Abramowicz 1999; Stone, Pringle & Begelman 1999; Stone & Pringle 2001; Machida et al. 2001; Hawley & Balbus 2002). The main difference between our work and these studies is that the other authors adopt the point of view that virtually all of the material at large radii has too much angular momentum to be accreted without the transport of angular momentum. They assume that material with zero or very low angular momentum is unimportant dynamically, and that accretion is dominated by angular momentum and energy transport processes. For example, for their initial conditions Stone et al. (1999) and Hawley & Balbus (2002) adopted a bounded torus in hydrostatic equilibrium with constant angular momentum, embedded in zero angular momentum ambient gas which is also in hydrostatic equilibrium. Thus, these calculations were set up so that, if not for the transport of angular momentum, there would be neither time evolution nor mass accretion. We recognize that transport processes are essential, but assert that the zero or very low angular momentum material also deserves a rigorous treatment because it can play an important role in determining the

total mass supply and accretion rate.

In this paper, we consider a far simpler case of an accretion flow than those occurring in nature (see Section 4). For example, we neglect viscosity and MHD effects. In particular, the MRI has been shown to be a very robust and universal mechanism to produce turbulence and the transport of angular momentum in disks at all radii (Balbus & Hawley 1998).

The outline of this paper is as follows. We describe our calculations in Section 2. In Section 3, we present our results. We summarize our results and discuss them together with their limitations in Section 4.

## 2. Method

### 2.1. Hydrodynamics

To calculate the structure and evolution of an accreting flow, we solve the equations of hydrodynamics

$$\frac{D\rho}{Dt} + \rho \nabla \cdot \mathbf{v} = 0, \quad (7)$$

$$\rho \frac{D\mathbf{v}}{Dt} = -\nabla P + \rho \nabla \Phi, \quad (8)$$

$$\rho \frac{D}{Dt} \left( \frac{e}{\rho} \right) = -P \nabla \cdot \mathbf{v}, \quad (9)$$

where  $\rho$  is the mass density,  $P$  is the gas pressure,  $\mathbf{v}$  is the velocity, and  $e$  is the internal energy density. We adopt an adiabatic equation of state  $P = (\gamma - 1)e$ , and consider models with  $\gamma = 5/3$ . Our calculations are performed in spherical polar coordinates  $(r, \theta, \phi)$ . We assume axial symmetry about the rotational axis of the accretion flow ( $\theta = 0^\circ$ ).

We present simulations using the pseudo-Newtonian potential  $\Phi$  introduced by Paczyński & Wiita (1980)

$$\Phi = -\frac{GM}{r - R_S}. \quad (10)$$

This potential approximates general relativistic effects in the inner regions, for a nonrotating black hole. In particular, the Paczyński–Wiita potential reproduces the last stable circular orbit at  $r = 3R_S$  as well as the marginally bound orbit at  $r = 2R_S$ .



## 2.2. Initial conditions and boundary conditions

For the initial conditions we adopt a Bondi accretion flow with zero angular momentum everywhere except for the outermost part of the flow. In what follows we briefly review the basics of Bondi accretion that allow us to specify details of our initial and boundary conditions as well as to interpret our results.

The Bernoulli function can be written as

$$B = H + \frac{v_r^2 + v_\theta^2}{2} + \frac{l^2}{2r^2 \sin^2 \theta} + \Phi, \quad (11)$$

where  $H$  is the enthalpy and  $l = v_\phi r \sin \theta$  is the specific angular momentum. For a polytropic equation of state  $P = K\rho^\gamma$ , the polytropic constant can be expressed as  $K = \rho_\infty^{1-\gamma} c_\infty^2 / \gamma$ , where  $c_\infty$  is the sound speed at infinity [i.e.,  $c_\infty^2 \equiv (dP/d\rho)_\infty$ ]. Therefore the enthalpy becomes

$$H = \int_{\rho_\infty}^{\rho} \frac{dP}{\rho} = \frac{\gamma}{\gamma-1} \left( \frac{P}{\rho} - \frac{P_\infty}{\rho_\infty} \right) = \frac{1}{\gamma-1} c_\infty^2 \left[ \left( \frac{\rho}{\rho_\infty} \right)^{\gamma-1} - 1 \right]. \quad (12)$$

Let us consider spherically symmetric, steady-state Bondi accretion onto an object with a Paczyński–Wiita (PW, hereafter) potential. In such a case,  $v_\theta = l = 0$  and the Bernoulli function simplifies to

$$B = -\frac{GM}{r - R_S} + \frac{c_\infty^2}{\gamma-1} \left[ \left( \frac{\rho}{\rho_\infty} \right)^{\gamma-1} - 1 \right] + \frac{v_r^2}{2} = 0. \quad (13)$$

Introducing dimensionless variables  $\alpha = \rho/\rho_\infty$ ,  $x = r/R_B$ ,  $R'_S = R_S/R_B$ , and  $u_r = v_r/c_\infty$ , we rewrite eq. (13) as

$$B' = -\frac{1}{x - R'_S} + \frac{1}{\gamma-1} (\alpha^{\gamma-1} - 1) + \frac{u_r^2}{2} = 0. \quad (14)$$

The transonic solution of the Bondi problem yields the sonic point at

$$x_s = \frac{5 - 3\gamma + 8R'_S + \sqrt{\Delta}}{8}, \quad (15)$$

where

$$\Delta = (5 - 3\gamma + 8R'_S)^2 - 64(1 - \gamma + R'_S)R'_S. \quad (16)$$

The dimensionless mass accretion rate  $\lambda \equiv x^2 \alpha u_r$  for the transonic solution can be calculated as

$$\lambda = x_s^2 \alpha_s u_{r,s} = x_s^2 \alpha_s^{(\gamma+1)/2}, \quad (17)$$

with the dimensionless density at the sonic point,  $\alpha_s$ , given by

$$\alpha_s = \left[ \frac{1}{2} + \frac{2(x_s - R'_S)}{x_s} - \frac{\gamma}{2} \left( 4 \frac{x_s - R'_S}{x_s} - 1 \right) \right]^{-1/(\gamma-1)}. \quad (18)$$

For  $\gamma = 5/3$ , the dimensionless sonic radius and mass accretion rate are

$$x_s = R'_S + \sqrt{2R'_S/3} \quad (19)$$

and

$$\lambda = \left( \frac{3}{4} R'_S \right)^2 \left( 1 + \sqrt{\frac{2}{3R'_S}} \right)^4, \quad (20)$$

respectively. Note that, for the PW potential as well as the fully general relativistic problem (Begelman 1978), Bondi flow with  $\gamma = 5/3$  has a sonic point at roughly the geometrical mean between the Bondi radius and the Schwarzschild radius. This is in contrast to the purely Newtonian case in which  $x_s = (5 - 3\gamma)/4 \rightarrow 0$  as  $\gamma \rightarrow 5/3$ .

We will use the results for Bondi accretion with the PW potential [i.e., equations (17)-(20)] as a reference point for analyzing our results and to set the initial conditions. Namely, we adopt  $v_\theta = 0$  while  $v_r$  and  $\rho$  are computed using the Bernoulli function and mass accretion rate  $\dot{M}_B \equiv -4\pi r^2 \rho v_r = \lambda 4\pi R_B^2 \rho_\infty c_\infty$ . We set  $\rho_\infty = 1$  and specify  $c_\infty$  through  $R'_S$  (note that  $R'_S = 2c_\infty^2/c^2$ ). We complete specification of the initial conditions by adopting a non-zero specific angular momentum  $l$  for  $r \geq x_s R_B$ . We also ran a few models in which the specific angular momentum initially is non-zero only at the outer radial boundary  $r_o$ . We found that, except for the initial transient, models with these initial conditions for  $l$  give the same results. However, adopting a non-zero specific angular momentum  $l$  for  $r \geq x_s R_B$  reduces the computational time significantly because the initial transient lasts for a much shorter time.

We consider a general case where the angular momentum depends on the polar angle via

$$l(r_o, \theta) = l_0 f(\theta), \quad (21)$$

with  $f = 1$  on the equator ( $\theta = 90^\circ$ ) and  $f = 0$  at the poles ( $\theta = 0^\circ$  and  $180^\circ$ ). We express the angular momentum on the equator as

$$l_0 = \sqrt{R'_C} R_B c_\infty, \quad (22)$$

where  $R'_C$  is the ‘‘circularization radius’’ on the equator in units of  $R_B$  for the Newtonian potential (i.e.,  $GM/r^2 = v_\phi^2/r$  at  $r = R'_C R_B$ ).

We adopt three forms for the function  $f(\theta)$ :

$$f_1(\theta) = 1 - |\cos \theta|, \quad (23)$$

$$f_2(\theta) = 1 - \cos^{10} \theta, \quad (24)$$

and

$$f_3(\theta) = \begin{cases} 0 & \text{for } \theta < \theta_o \text{ and } \theta > 180^\circ - \theta_o \\ l_0 & \text{for } \theta_o \leq \theta \leq 180^\circ - \theta_o. \end{cases} \quad (25)$$

Our choice of the  $\theta$  dependence of  $l$  at infinity is motivated by the following: the  $l$  distribution described by eq. (23) allows us to study a case in which the flow at large radii is very similar to the Bondi flow as the material with  $l > 2R_S c$  is confined to within a narrow range of  $\theta$  above and below the equator if  $l_0$  is close to  $2R_S c$ . In such a case most of the material at large radii has  $l < 2R_S c$  and can be accreted, in principle. On the other hand, the  $l$  distribution described by eqs. (24) or (25) allows us to study the opposite case, in which the material with  $l > 2R_S c$  at large radii occupies nearly the entire range of  $\theta$  above and below the equator, even if  $l_0$  is not much larger than  $2R_S c$ . Then most of the material at large radii has  $l > 2R_S c$ ; only in a narrow polar region is  $l$  low enough for accretion to take place ( $l < 2R_S c$ ). We note that for the  $\theta$  dependence of  $l$  described by  $f_1$  and  $f_2$ , we calculate  $\theta_0$  using eq. (6) and an assumed value for  $l_0$ . For the  $\theta$  dependence of  $l$  described by  $f_3$ ,  $l_0$  as well as  $\theta_0$  are free parameters.

Our standard computational domain is defined to occupy the radial range  $r_i = 1.5 R_S \leq r \leq r_o = 1.2 R_B$  and the angular range  $0^\circ \leq \theta \leq 180^\circ$ . We consider models with  $R'_S$  from  $10^{-2}$  to  $10^{-3.5}$ . The  $r - \theta$  domain is discretized into zones. For  $R'_S = 10^{-2}$ ,  $10^{-3}$ , and  $10^{-3.5}$ , our numerical resolution consists of 100, 140, and 160 zones in the  $r$  direction, respectively. In the  $\theta$  direction, our numerical resolution consists of 100 zones for all values of  $R'_S$ . We usually fix zone size ratios,  $dr_{k+1}/dr_k = 1.05$ ,  $d\theta_l/d\theta_{l+1} = 1.05$  for  $0^\circ \leq \theta \leq 90^\circ$  (i.e., the zone spacing is decreasing in this region) and  $d\theta_{l+1}/d\theta_l = 1.05$  for  $90^\circ \leq \theta \leq 180^\circ$ . For runs with very high  $l_0$  we adopt  $d\theta_l/d\theta_{l+1} = 1.0$  for  $0^\circ \leq \theta \leq 180^\circ$  (see section 3.3). For runs with a very narrow funnel in which we use a step function for  $f(\theta)$ , we adopt  $d\theta_{l+1}/d\theta_l = 1.03$  for  $0^\circ \leq \theta \leq 90^\circ$  (i.e., the zone spacing is increasing in this region) and  $d\theta_l/d\theta_{l+1} = 1.03$  for  $90^\circ \leq \theta \leq 180^\circ$ .

The boundary conditions are specified as follows. At the poles, (i.e.,  $\theta = 0^\circ$  and  $180^\circ$ ), we apply an axis-of-symmetry boundary condition. For the inner and outer radial boundaries, we apply an outflow boundary condition. Our choice for the location of the inner radial boundary,  $r_i = 1.5R_S$ , ensures that the flow near this boundary is supersonic and the outflow condition is appropriate. To represent steady conditions at the outer radial boundary, during the evolution of each model we continue to apply the constraints that in the last zone in the radial direction,  $v_\theta = 0$ ,  $v_\phi = l_0 f(\theta)/r \sin \theta$ , and the density is fixed at the Bondi value at all times. Note that we allow  $v_r$  to float. We have found that this technique, when applied to calculations of spherically symmetric accretion, produces a solution that relaxes to the steady-state Bondi solution for  $l = 0$ . For non-zero  $l$ , we find

that the outer radial boundary must be sufficiently far from the circularization radius to ensure that the assumption of pure radial flow (i.e.,  $v_\theta(r_o) = 0$ ) does not change the solution (see Section 3).

To solve eqs. (7)-(9) we use the ZEUS-2D code described by Stone & Norman (1992), modified to implement the PW potential. As with all Eulerian codes, one ought to test how much numerical diffusion error (“numerical viscosity”) affects the results. In particular, shocks are captured with a standard quadratic artificial viscosity (see Stone & Norman 1992). Since we compute the evolution of adiabatic flows without any physical viscosity, numerical effects can, in principal, limit the accuracy of the results. The artificial viscosity, which is not shown in our equations (7)-(9), is present only when the (inward) velocity divergence is nonvanishing. When present, artificial viscosity heats the gas and transports angular momentum. As a test, we reran model A04fl1a with a resolution of 150 in the  $r$  direction and of 200 in the  $\theta$  direction (i.e., the resolution of the test run is twice that in model A04fl1a in both directions). We found that the mass accretion rate in model A04fl1a and its higher resolution counterpart agree to within one part in  $10^3$ . As for heating of the gas due to artificial viscosity, we found that the polytropic constant,  $K$ , is conserved in all of our simulations, except for departure of  $\lesssim 1\%$  near the equator for small radii, where weak shocks appear. We conclude that our numerical simulations treat inviscid flows satisfactorily.

### 3. Results

Our numerical models are specified by several parameters. The length scale is determined by the black hole radius in units of the Bondi radius,  $R'_S$ . Our second parameter is the adiabatic index,  $\gamma$ . The last parameter (or a function rather) is the angular momentum at the outer radial boundary,  $l = l_0 f(\theta)$ .

In real systems,  $R'_S$  is relatively small ( $10^{-8} \lesssim R'_S = 2c_\infty^2/c^2 \lesssim 10^{-5}$ ) because the sound speed at large distances from a black hole is very small compared to the speed of light. Models with so great a radial domain would be very demanding computationally. We therefore decided to explore the main features of our model by considering a smaller radial domain,  $10^{-3.5} \leq R'_S \leq 10^{-2}$ . We consider adiabatic flows with  $\gamma = 5/3$ . Finally, we assume an angular momentum distribution at the outer radial boundary as described in Section 2. We focus our attention on accretion of matter with low angular momentum, i.e., where the

corresponding centrifugal force is small compared to gravity for all  $\theta$  at the Bondi radius:

$$\frac{l_0^2 f^2(\theta)}{R_B^3 \sin^2 \theta} < \frac{GM}{(R_B - R_S)^2}. \quad (26)$$

In the limit  $R_B \gg R_S$  and using our definition of  $R'_C$ , we can rewrite the above equation as

$$\frac{f^2(\theta)}{\sin^2 \theta} < \frac{1}{R'_C}. \quad (27)$$

Table 1 summarizes the properties of the simulations we discuss here. Columns (2) through (7) give the numerical resolution in the radial direction; the black hole radius compared to the Bondi radius,  $R'_S$ ; the circularization radius compared to the Bondi radius,  $R'_C$ ; the specific angular momentum on the equator at  $r = r_o$ ,  $l_0$ , in units of  $2R_{Sc}$ ; the width of the angular distribution for which  $l \leq 2R_{Sc}$ ,  $\theta_o$ ; and the angular momentum dependence on the polar angle at the outer boundary,  $f(\theta)$ , respectively. Table 1 also presents the final time at which we stopped each simulation (all times here are in units of the Keplerian orbital time at  $r = R_B$ ), the maximum specific angular momentum at the inner radial boundary,  $l_a^{max}$ , and the time-averaged mass accretion rate through the inner radial boundary measured near the end of the simulation, in units of the corresponding Bondi accretion rate. Finally, column (11) gives comments about runs different from the standard runs (e.g., the outer radial boundary set at  $12R_B$  instead of  $1.2R_B$ )

Our simulations show that for  $l_0 > 2R_{Sc}$  the accretion flow consists of a thick, equatorial torus where the material has too much angular momentum to be accreted, and a supersonic polar funnel where the material has  $l$  low enough to be accreted. We describe an example of such an accretion flow in some detail first (Section 3.1). This is followed by a limited parameter survey in which we focus on varying three key aspects of our models: the maximum angular momentum for a given distribution, the angular distribution of angular momentum on the outer boundary, and the black hole radius compared to the Bondi radius.

### 3.1. Accretion flow consisting of a torus and a funnel

In this section we describe the properties and behavior of our model in which  $R'_S = 10^{-3}$ ,  $R'_C = 10^{-1}$ , and  $f(\theta) = 1 - |\cos \theta|$  (model B04f1a). For the above parameters, the specific angular momentum on the equator at the outer boundary is  $\sim 3.5$  in units of  $2R_{Sc}$ , thus the material that cannot be accreted onto the black hole is located relatively close to the equator,  $45^\circ \leq \theta \leq 135^\circ$  at the outer boundary.

Figure 1 presents a sequence of specific angular momentum contours and velocity fields for model B04f1a. The length of the arrows in the lower panels is proportional to the poloidal velocity  $\sqrt{v_r^2 + v_\theta^2}$ . As we mentioned in Section 1, after a transient episode of infall, the gas with  $l > 2R_{SC}$  piles up outside the black hole and settles into a thick torus bounded by a centrifugal barrier near the rotation axis. The low- $l$  material close to the axis accretes almost steadily through a funnel. The distribution of specific angular momentum in the torus becomes increasingly homogeneous as material with  $l \sim 0.9$  replaces material with higher  $l$ . The flow in the torus is subsonic, variable and is directed outward near the equator and inward close to the poles. There is no symmetry with respect to the equator. The time-dependence persists even after  $t_f=9$ . Thus, a meridional circulation is established in the torus. However, it is important to note that the time-averaged gross properties of the flow (such as the mass accretion rate and the shape of the torus and funnel) settle down to a steady state.

To show the accretion flow in more detail, Figure 2 presents the enlargement of two panels from Figure 1 (the panels from the the end of our simulations). This figure shows also the radial sonic surface, that is, the location where the radial Mach number ( $M_r \equiv v_r/c_s$ ) equals one. Note that the specific angular momentum in the torus for small radii is nearly constant ( $l \sim 1$  in units of  $2R_{SC}$ ). Additionally, for small radii the sonic surface approximately coincides with the  $l \approx 0.9 \times 2R_{SC}$  surface. The ‘south’ lobe of the sonic surface is more elongated than the ‘north’ lobe at the end of the simulations. However, in a time-averaged sense both lobes are very similar.

Next we consider the angular dependence of the flow at small radii. Figure 3 is a plot of the angular dependence of the Mach number, specific angular momentum and mass flux density at  $r = r_i = 1.5R_S$ . This figure shows three important features of the accretion flow: (i) the accretion flow is highly supersonic in the radial direction, (ii)  $l_a^{max}$  is not  $2R_{SC}$  but rather somewhat smaller ( $0.9 \times 2R_{SC}$ ) and (iii) the mass flux density is a strong function of the polar angle: it is nearly flat near the poles and peaks near the equator where  $l \approx 0.6$  in units of  $2R_{SC}$ .

To provide more insight into the character of the accretion flow, Figure 4 shows the angular dependence of flow properties on the sonic surface (the  $M_r = 1$  surface). The top panel shows the radius at which  $M_r = 1$ ,  $r_s$ . The second panel from the top shows the specific angular momentum and the latitudinal Mach number,  $M_\theta \equiv v_\theta/c_s$ . The second panel from the bottom and the bottom panel show, respectively, the mass flux density ( $\rho v_r$ ) and a measure of how much the flow deviates from a purely radial flow at the sonic surface,  $\Delta\theta$ . We define  $\Delta\theta$  as the difference between a given polar angle,  $\theta$ , on the sonic surface, and the polar angle at which the gas with a given  $l$  originated at  $r = r_o$ . Because our models

conserve specific angular momentum along streamlines,  $\Delta\theta$  can be formally estimated as

$$\Delta\theta(\theta) = \theta - f^{-1}(l(r_s, \theta)/l_0), \quad (28)$$

for  $0^\circ \leq \theta \leq 90^\circ$  and

$$\Delta\theta(\theta) = 180^\circ - \theta - f^{-1}(l(r_s, \theta)/l_0), \quad (29)$$

for  $90^\circ \leq \theta \leq 180^\circ$ .

Figure 4 shows that the sonic radius is the highest along the poles, comparable to the Bondi sonic radius [see eq. (19)] and decreases by approximately an order of magnitude near the equator (see also Figure 2). Additionally, Figure 4 shows that the flow deviates from radial flow on the sonic surface. The deviation from radial flow increases with increasing angle from the poles. For angles from the poles  $\lesssim 30^\circ$ , the deviation is small and the radial approximation holds. However, the mass flux density is dominated by matter originating at angles from  $> 40^\circ$  from the poles, for which the deviation from radial flow can be large (i.e.,  $10^\circ < \Delta\theta < 50^\circ$ ). We note that the total mass accretion rate is dominated by streamlines which deviate only moderately from radial flow on the sonic surface. This conclusion is based on the observation that  $\Delta\theta \lesssim 10^\circ$  for material with  $l \sim 0.6 \times 2R_{SC}$ .

Finally, to provide some insight into the time dependence, Figure 5 shows the time evolution of the mass accretion rate in units of the corresponding Bondi rate. Initially,  $\dot{M}_a$  drops from 1 to 0.23 at  $t = 0.25$ . Then it starts oscillating around 0.3 with an amplitude of  $\sim 0.1 \dot{M}_a/\dot{M}_B$ .

### 3.2. Dependence of accretion flow properties on $l_0$

To check the trends of the accretion flow with the main model parameters, we have performed a limited parameter survey. We first describe our results for models with all parameters the same as in model B04f1a except for  $l_0$ .

The main result from our runs with various  $l_0$  is that the mass accretion rate does not depend on this parameter (see Table 1), within the constraints imposed by assuming low angular momentum at  $R_B$  [eq. (27)]. The basic reason for this result is the fact that the properties of the accretion flow are determined by the geometry of the torus, which has a uniform specific angular momentum slightly larger than the maximum  $l$  of the accreted gas. The material with  $l \gtrsim 2R_{SC}$  inflows in the polar region, turns around as it reaches a centrifugal barrier, and then starts to outflow along the equator. As a result, a thick

torus forms with gas of the highest angular momentum ( $l \approx l_0 > 2R_{Sc}$ ) near the equator being replaced by gas of lower angular momentum ( $l \gtrsim 2R_{Sc}$ ). The geometry of the polar region, where material is accreted (the funnel) and the mass accretion rate through it are constrained by the shape of the torus.

To illustrate the insensitivity of the inner flow to the angular momentum at large radii, Figure 6 shows the angular momentum contours for our model B01f1a at  $t_f = 3.5$ . For this model we assumed  $l_0 = 2R_{Sc}$  so that in the purely radial case all material should be accreted. However, the flow converges toward the equator, and gas pressure effects allow only the material with  $l_0 \lesssim 0.87 \times 2R_{Sc}$  to be accreted. The material with higher  $l$  turns around and forms a thick torus with properties very similar to those of model B04f1a, which has a much higher  $l$  at large radii. Comparing the left-hand panel of Figure 6 with the top panels of Figure 1 shows clearly how different the angular momentum distributions are at large radii in these two runs. However, comparing the right-hand panel of Figure 6 with the left-hand panel of Figure 2 shows that the angular momentum distribution at small radii, the shape of the torus (the  $l = 0.9$  contour) as well as the sonic surface are qualitatively similar for both runs.

We conclude that the relative insensitivity of the torus to the angular momentum distribution at infinity is responsible for the fact that  $\dot{M}_a$  does not depend on  $l_0$  and that the geometrical argument we used in Section 1 is invalid. As runs B04f1a and B01f1a illustrate, the width of the  $l$  distribution for  $l < 2R_{Sc}$  at infinity does not control the mass accretion rate. Even if material with low  $l$  comes from close to the equator it still has to go ‘around’ the inner torus. We suggest that a more useful way of geometrically determining the mass accretion rate is to compare the angle between the torus upper envelope and the pole,  $\theta_t$ , and the width of the angular distribution for which  $l \sim 2R_{Sc}$ ,  $\theta_o$ . However, such a method of determining  $\dot{M}_a$  poses the difficulty that  $\theta_t$  depends on radius and we need to know at what radius we have to measure  $\theta_t$ .

### 3.3. Dependence of accretion flow properties on the angular distribution of $l$

Motivated by the conclusion from the previous section, we have performed a few simulations using an angular distribution for  $l$  that yields a smaller value of  $\theta_o$  than that given by  $f_1$  (see eq. 23), for a given  $l_0$ . We wish to check whether the insensitivity of  $\dot{M}_a$  to  $l_0$ , as described above, holds in cases where  $\theta_o$  is small, in particular when  $\theta_o < \theta_t$ .

Inspection of the expression (27) shows that there are three possible ways of decreasing  $\theta_o$  within the constraints imposed by the assumption of low angular momentum: (i) reduce



$R'_C$  by increasing  $R_B$  for given  $R_C$  and  $R_S$  and increase  $l_0$  at the same time, (ii) choose a function  $f(\theta)$  that increases with increasing  $\theta$  very quickly for small  $\theta$  and very slowly for larger  $\theta$ , or (iii) both. We will be able to explore the first possibility only in a limited way (see next section) because, as we mentioned above, models with  $R_B$  very high compared to  $R_S$  are very demanding computationally. However, we can explore the second possibility at relatively low computational cost for moderate  $R_B$ .

As before, we consider in detail only one example: for our model B08f2a, all parameters are the same as for model B04f1a with the exceptions that  $l$  scales with  $\theta$  at  $r_o$  as  $1 - \cos^{10} \theta$  and  $d\theta_l/d\theta_{l+1} = 1$ . Such a flat distribution of  $l$  for high  $\theta$  reduces the size of the polar region where  $l < 2R_{Sc}$  (i.e., the  $\theta_o$  angle). Thus, we expect that  $\theta_o < \theta_t$  in this case and the mass accretion rate will be lower than in model B04f1a. Indeed, we find that  $\dot{M}_a$  in model B08f2a is lower than that for model B04f1a by a factor of  $\sim 3$ . We observe a similar reduction of  $\dot{M}_a$  for all runs using  $f_2$  compared to runs using  $f_1$ , regardless of  $R_S/R_B$ .

Our experiments with various  $l_0$  and angular distributions of  $l$  show that  $\theta_o$  appears to be the key parameter that determines the effect of the angular momentum at the outer boundary on the mass accretion rate through the inner boundary. To illustrate the role of  $\theta_o$ , Figure 7 plots the mass accretion rate as a function of  $\theta_o$  for all our runs with  $R_S/R_B = 10^{-3}$ , without making any distinction between models with different  $f(\theta)$  and/or  $l_0$ . Figure 7 shows one of the key results of this paper. For large  $\theta_o$  — corresponding to a broad funnel at  $R_B$  —  $\dot{M}_a$  is constant, whereas for small  $\theta_o$  — corresponding to a narrow funnel at  $R_B$  —  $\dot{M}_a$  decreases with decreasing  $\theta_o$ .

Figure 7 also compares our numerical results (the solid line) with the simple prediction, eq. (5) (the dashed line). Equation (5) predicts that  $\dot{M}_a$  decreases monotonically with decreasing  $\theta_o$  for all  $\theta$ . Generally, our prediction from Section 1 overestimates  $\dot{M}_a$  for large  $\theta_o$  and underestimates  $\dot{M}_a$  for small  $\theta_o$ . The decrease of  $\dot{M}_a$  with decreasing  $\theta_o$  shown in our numerical simulations is consistent with the theoretical prediction, but only qualitatively and only in the limit of a narrow funnel.

We note that in the limit of a narrow funnel the sonic radius increases with decreasing  $\theta_o$ . We can understand the  $\dot{M}_a$  vs.  $\theta_o$  relation in the limit of a narrow funnel by combining this increase in the sonic radius with two other facts: (i) the solid angle subtended by the accretion funnel decreases with increasing radius and (ii) the solid angle subtended by the accretion funnel is greater than  $\Delta\Omega_o$  ( $\Delta\Omega_f = \Delta\Omega_o$  at  $r_o$  by definition). Thus,  $\Delta\Omega_f$  and consequently  $\dot{M}_a$  decrease with decreasing  $\theta_o$ . This explains why the decrease of  $\dot{M}_a$  with decreasing  $\theta_o$  shown in our numerical simulations is qualitatively consistent with the theoretical prediction. The explanation for the quantitative difference is simply related to the second fact listed above, i.e.,  $\Delta\Omega_f \geq \Delta\Omega_o$  at the sonic radius,  $r_s < r_o$ .

### 3.4. Dependence of accretion flow properties on $R_S/R_B$ and $r_o$

The most difficult parameters of our models to explore are the  $R_S/R_B$  ratio and the outer radius of the computational domain. As mentioned earlier, we have to consider values of  $R_S/R_B$  orders magnitude larger than those found in astrophysical objects. Similarly, exploring a wide range of  $r_o$  is computationally prohibitive. Therefore we have performed only a few simulations in which we vary these parameters. We check then whether our results allow us to extrapolate an  $\dot{M}$  vs.  $R_S/R_B$  relation to very low values of  $R_S/R_B$ .

Our results from the runs with various  $r_o$  allow us to make a few observations. First, a proper study of Bondi accretion with low angular momentum requires  $R_S/R_B < 10^{-2}$ . For  $R_S/R_B = 10^{-2}$  or larger, the assumption of low angular momentum (eq. 27) is valid only for a very narrow range of  $l_0$  while the assumption of radial flow at the outer boundary is valid only for  $r_o$  much larger than the Bondi radius. For example, our models A03f1a and A03f1b show that the location of the outer boundary can change the solution dramatically for  $R_S/R_B < 10^{-2}$  and moderate  $l_0$  of  $2.5 \times 2R_{Sc}$ . For these parameters the circularization radius is relatively high,  $R'_C = 0.5$ , and the assumption that the flow is radial close to the Bondi radius is not valid. Our models A03f1a and A03f1b differ only in the location of the outer radial boundary,  $r_o = 1.2R_B$  and  $12 R_B$ , respectively. However, this difference produces dramatic change in the accretion flow. For model A03f1b, the flow is non-radial even as far as the Bondi radius and material with  $l$  as low as  $\sim 0.4 \times 2R_{Sc}$  turns around near the equator and never makes it through the inner boundary. Since the point where this material turns is relatively far from the inner boundary, the sonic surface of the flow coming from the polar region is approximately spherical and almost as large as the sonic surface in Bondi accretion with  $l = 0$ . *Because of these properties of the sonic surface the mass accretion rate is almost as high as the Bondi rate!* This model once again demonstrates that the mass accretion rate is determined more by the shape of the flow that does not accrete than by the angular distribution of  $l$  at large radii. On the other hand, model A03f1a has  $r_o = 1.2$  and forces the flow to be radial near the Bondi radius via our outer boundary conditions. Therefore, the flow converges toward the equator at smaller radii and the material that goes through the inner boundary has  $l$  higher than in the model A03f1b. Additionally, the point where the material with too high  $l$  turns around near the equator is closer to the black hole than the sonic point in the polar region. Consequently, for model A03f1a the sonic surface has the ‘figure-8’ shape and the mass accretion rate is lower than the Bondi rate.

Because of the sensitivity of the results to the location of the outer boundary for models with  $R_S/R_B = 10^{-2}$ , we do not consider these models in great detail. However, we note that these models (with fixed  $r_o$ ) show an  $\dot{M}_a$  vs.  $l$  relation very similar to the one we

found for models with  $R_S/R_B = 10^{-3}$ .

We base most of our observations and conclusions on models with  $R_S/R_B = 10^{-3}$  not only because they are computationally affordable but also because they do not depend on the location of the outer boundary. Comparing models B04f1a and B04f1b we find that moving  $r_o$  from  $1.2 R_B$  to  $12 R_B$  does not change the solution for the accretion flow. The reason for this is simply that, contrary to models with  $R_S/R_B = 10^{-2}$ , the Bondi radius is large enough compared to  $R_C$  that the  $\theta$  component of centrifugal force is relatively small. Consequently, the radial approximation at the Bondi radius is valid for models with  $R_S/R_B = 10^{-3}$ .

Unfortunately, models with the ratio  $R_S/R_B$  lower than  $10^{-3}$  are computationally too expensive to be explored as fully as models with  $R_S/R_B = 10^{-3}$ . For example, it takes about three weeks of CPU time on a modern workstation to run one model with  $R_S/R_B = 10^{-3.5}$  for 3 dynamical time scales at the Bondi radius. Therefore, we limited ourselves to two models with  $10^{-3.5}$ , model C04f1a and C08f2a. Our primary goal of running these models was to check whether the mass accretion rate would change compared to models with  $R_S/R_B = 10^{-3}$ .

Model C04f1a is meant to represent a model with a wide accretion funnel (the second regime in the  $\dot{M}_a$  vs.  $l$  relation) while model C08f2a is meant to represent a model with a narrow accretion funnel (the third regime in the  $\dot{M}_a$  vs.  $l$  relation). For model C04f1a, the mass accretion rate is smaller than the corresponding model with  $R_S/R_B = 10^{-3}$  (i.e., model B04f1a, see Table 1) but we note that the mass accretion rate was increasing with time at the end of our calculations. Judging from the trend of  $\dot{M}_a$  with time we conclude that the mass accretion rate does not change much when the ratio  $R_S/R_B$  decreases from  $10^{-3}$  to  $10^{-3.5}$  in the wide funnel case. We reach the same conclusion for the models in the narrow funnel case. We recognize that our conclusions are based on very limited data but they are consistent, at least for small  $R_S/R_B$ , with our understanding of how the mass accretion rate is determined.

## 4. Discussion

This paper presents the first phase of our study of slightly rotating accretion flows onto black holes. We decided to consider a far simpler case of an accretion flow than those occurring in nature. In particular, we neglected the gravitational field due to the host galaxy, radiative heating and cooling, viscosity and MHD effects. Perhaps the

most important simplification we made is neglecting the transport of energy and angular momentum outward as needed to accrete matter with a specific angular momentum higher than  $2R_{SC}$ . Nevertheless, our results provide a useful exploratory study of accretion onto black holes as they have revealed unexpected properties and complexity of accretion flows in even this simple case. Clearly, a lot more work is needed to give a definitive answer to the question of whether slow rotation of gas at large radii is really enough to reduce the mass accretion rate to the level required by observations. In what follows we will summarize our results, briefly review the limitations of our work, and discuss how the physical effects neglected here may change the results.

We have performed numerical 2D, axisymmetric, hydrodynamical simulations of slightly rotating, inviscid accretion flows onto a black hole. We attempt to mimic the boundary conditions of classic Bondi accretion flows with the only modifications being the introduction of a small, latitude-dependent angular momentum at the outer boundary and a pseudo-Newtonian gravitational potential. The distribution of  $l$  with latitude allows the density distribution at infinity to approach spherical symmetry. The main result of our calculations is that the properties of the accretion flow do not depend as much on the outer boundary conditions (i.e., the amount as well as distribution of the angular momentum) as on the geometry of the *non-accreting matter*. Additionally, we find that the mass accretion rate *vs.* angular momentum relation for a given angular distribution of  $l$  has three regimes: (i) for low  $l$  (i.e.,  $l < 2R_{SC}$  for all  $\theta$  at large radii), a torus does not form and  $\dot{M}_a = \dot{M}_B$ , (ii) for intermediate  $l$ , or more appropriately where there is a narrow range of  $\theta$  for which  $l > 2R_{SC}$  so that  $\theta_o > \theta_t$ ,  $\dot{M}_a \sim const$  and (iii) for high  $l$ , or in the case for which  $l > 2R_{SC}$  at nearly all  $\theta$  so that  $\theta_o < \theta_t$ ,  $\dot{M}_a$  decreases with increasing  $l_0$ . Our limited data suggest that in the second regime, the actual value of the constant is dependent on the ratio  $R_S/R_B$  for large  $R_S/R_B$  but becomes independent on the ratio for small  $R_S/R_B$  (i.e., for  $R_S/R_B \lesssim 10^{-3}$ ). We conclude that the inclusion of even slow rotational motion of the inviscid flow at large radii can significantly reduce  $\dot{M}_a$  compared to the Bondi rate, as the  $\dot{M}_a$  *vs.*  $l$  relation in the third regime indicates. For  $R_S/R_B \geq 10^{-3.5}$ , our results show that  $\dot{M}_a$  can be reduced by  $\sim 1.5$  orders of magnitude compared to the Bondi rate. To reduce the mass accretion rate more, the accretion funnel needs to be much narrower than the funnels allowed by our assumption of low angular momentum (eq. 27) for  $R_S/R_B \geq 10^{-3.5}$ . It remains to be seen whether simulations for values of  $R_S/R_B$  as low as those observed in astrophysical systems (i.e.,  $R_S/R_B \lesssim 10^{-6}$ ) will confirm our predictions that the accretion funnel can be very narrow and subsequently the mass accretion rate very small.

We note that the discontinuous change from quasi-spherical to a disk-like flow was first found by Abramowicz & Zurek (1981). Abramowicz & Zurek studied analytically the adiabatic accretion of a radial flow onto a black hole using the PW potential. They

considered the case of constant specific angular momentum and also found that for small  $l$ , the flow is quasi-spherical and becomes transonic at  $x_s \gg R'_S$  while for sufficiently large  $l$ , the flow has a disk-like pattern and  $x_s \leq 3R'_S$ . Applying Abramowicz & Zurek's solution for the sonic point, we find very good agreement between the location of the sonic point on the equator and their prediction. In particular, for  $n \equiv 1/(\gamma - 1) = 3/2$ ,  $l = 2R_S c$ , and zero total energy, eq. 3.5 in Abramowicz & Zurek (1981) yields that the sonic point equals  $1 + \sqrt{3}$ , which is in a good agreement with our result for  $\theta = 90^\circ$  where the sonic radius is  $\approx 2.5R_S$  (e.g., see Figure 4). Our simulations also agree with Abramowicz & Zurek's result that the transition between quasi-spherical and disk-like accretion occurs at  $l \approx 2R_S c$ .

We find that the shape of the polar funnel through which matter is accreted is partially constrained by the torus, which is made of matter that cannot accrete. The torus consists of material with roughly uniform angular momentum and its structure does not depend much on the outer conditions. The accretion funnel is therefore also not very sensitive to the outer conditions in the limit that it is broad at large radii (i.e., large  $\theta_o$ ). This is the key reason for the insensitivity of  $\dot{M}_a$  to  $l$  in the second regime and its weak sensitivity in the third regime: the mass accretion rate depends on the geometry of the sonic surface at radii where the presence of the torus is important, and not only on the geometry at the outer boundary. Thus, the accretion flow in the funnel should depend on the physics that controls the flow in the torus. In particular, the introduction of energy dissipation, and the transport of energy and angular momentum in the torus, may change the shape of the torus and its effect on the polar regions, where material can accrete without the transport of angular momentum. One could argue that the total mass accretion rate (via both the funnel and torus) onto the black hole should increase when transport of angular momentum and consequently accretion via the torus are allowed. However, it is not clear by how much  $\dot{M}_a$  will increase, if at all, because the energy and angular momentum from the torus are likely to be deposited in the polar region (see e.g., Stone, Pringle & Begelman 1999; Blandford & Begelman 1999; Blandford & Begelman 2002a, 2002b; Hawley & Balbus 2002). Indeed, outflow from the torus may interfere with the inflow in the funnel and  $\dot{M}_a$  may well *decrease*. There is also a possibility that accretion via the funnel will decrease, not because of the dynamical effects due to outflowing material but because a torus in which energy is dissipated should be hotter and thicker than a torus in which energy cannot be dissipated. On the other hand, it is not clear how accretion via the torus will change when supersonic accretion in the funnel is present. Our simulations show that the range of  $\theta$  that is occupied by the accretion funnel increases with decreasing distance from the black hole. In particular, accretion through the inner radius occurs for the entire range of  $\theta$ . We expect that the presence of a supersonic accretion flow near the equator at small radii may cause accretion via the torus to be less effective compared to the situation in which the material

in the polar region is static. Most simulations of the formation of the torus have assumed that the material near the poles, outside the initially hydrostatic rotating torus, is static or subsonic, and therefore unimportant dynamically.

Even within our simple framework of inviscid flow, we anticipate that our results may change if we relax some of our assumptions about the geometry at the outer boundary. The assumptions we adopted are as simple as possible because we do not know the magnitude of the angular momentum of material in the environment of SMBHs, nor the angular distribution of  $l$ . In particular, it is rather unlikely that the  $l$  distribution is axisymmetric. Therefore, fully 3D calculations are required to explore how  $\dot{M}_a$  responds to non-axisymmetric  $l$  distributions. In the context of inviscid HD calculations similar to ours, one would expect that 3D effects may reduce  $\dot{M}_a$  compared to 2D axisymmetric calculations. For example, it is possible that rotation at large radii occurs not just around one axis but around two or more axes. It is also possible that rotation occurs around an axis that changes with  $r$ . Additionally it is plausible that there are “winds” flowing past the SMBH or that the entropy in the SMBH environment is variable. In such a case, material with too high  $l$  to be accreted may occupy nearly the entire range of  $\theta$  at small radii (near or inside the sonic radius) and prevent low- $l$  material from accreting. In terms of accretion funnels, this would correspond to the situation in which the ‘funnel’ is very narrow and maybe not lined up with a radial vector.

Perhaps the best studied massive black hole with a very low luminosity is the black hole in the Galactic center. Many models and ideas for how to explain very low SMBH luminosities have been explored in the context of Sgr A\*. In particular, Melia (1992; 1994) proposed a spherical accretion model in which the accretion flow is assumed to be in free-fall until a Keplerian disk is formed within a small circularization radius. Coker & Melia (2000) looked at the problem of spherical accretion but with the magnetic field being in subequipartition. The latter results in a reduced bremsstrahlung emissivity and can help to explain the low luminosity of Sgr A\*. A relatively small distance to Sgr A\* allows us to map the vicinity of the black hole at the Galactic center. The complexity of such maps (e.g., in radio) motivate three dimensional HD simulations. For example, Coker & Melia (1997) performed three-dimensional simulations of Bondi-Hoyle accretion of stellar winds onto a black hole. Clearly Sgr A\* shows us that accretion onto black holes is a complex phenomenon and the Bondi accretion formula should be used with great caution because the assumption of spherical accretion is most certainly an oversimplification.

We finish with the observation that after three decades of studying the Bondi problem with slight rotation at large radii (see, e.g., Henriksen & Heaton 1975, Lynden-Bell 1978; Cassen & Pettibone 1976; Sparke & Shu 1980; Sparke 1982; Abramowicz & Zurek 1981,

for analytic attempts to solve this problem and see references in Section 1 for 2D and 3D numerical simulations), we still find new complexities in the behavior of accretion flows. In our next phase of studying these flows, we will consider 3D MHD models of radiatively inefficient flows.

ACKNOWLEDGMENTS: We thank J.M. Stone for useful discussions. We acknowledge partial support from NSF grant AST-9876887. DP also acknowledges partial support from NASA grant NAG5-11736. Some computations were performed at Imperial College Parallel Computing Center.

## REFERENCES

- Abramowicz, M.A., Chen, X., Kato, S., Lasota, J.-P., Regev, O. 1995, *ApJ*, 438, L37
- Abramowicz, M.A., Igumenshchev, I. V., Quataert, E., & Narayan, R. 2002, *ApJ*, 565, 1101
- Abramowicz, M.A., & Zurek, W.H. 1981, *ApJ*, 246, 314
- Baganoff, et al. 2001, *ApJ*, submitted (astro-ph/0102151)
- Balbus, S.A., & Hawley, J.F. 1998, *Rev. Mod. Phys.*, 70, 1.
- Balbus, S.A., & Hawley, J.F. 2002, *ApJ*, 573, 749
- Begelman, M.C., 1978, *A&A*, 70, 583
- Begelman, M.C., & Meier, D.L. 1982, *ApJ*, 253, 873
- Blandford, R.D., & Begelman, M.C. 1999, *MNRAS*, 303, L1
- Blandford, R.D., & Begelman, M.C. 2002a, in preparation
- Blandford, R.D., & Begelman, M.C. 2002b, in preparation
- Bondi, H. 1952, *MNRAS*, 112, 195
- Cassen, P., & Pettibone, D. 1976, *ApJ*, 208, 500
- Chen, X., Taam, R.E., Abramowicz, M.A., & Igumenshchev, I.V. 1997, *MNRAS*, 285, 439
- Clarke, D., Karpik, S., & Henriksen, R.N. 1985, *ApJS*, 58, 81
- Coker, R.F., & Melia, F. 1997, *ApJ*, 488, L149
- Coker, R.F., & Melia, F. 2000, *ApJ*, 534, 723
- Di Matteo, T., Allen, S.W., Fabian, A.C., Wilson, A.S., & Young, A.J. 2002, *ApJ*, submitted (astro-ph/0202238)
- Di Matteo, T., Carilli, C.L., & Fabian, A.C. 2001, *ApJ*, 547, 731
- Di Matteo, T., Fabian, A.C., Rees, M.J., Carilli, C. L., & Ivison, R.J. 1999, *MNRAS*, 305, 492
- Di Matteo, T., Quataert, E., Allen, S.W., Narayan, R., & Fabian, A. C. 2000 *MNRAS*, 311, 507



- Hawley, J.F. 1986, in *Radiation Hydrodynamics in Stars and Compact Objects*, ed. D. Mihalas & K.-H. Winkler (New York:Springer), 369
- Hawley, J.F., & Balbus, S.A. 2002, *ApJ*, 573, 749
- Hawley, J.F., Balbus, S.A., & Stone, J.M. 2001, *ApJ*, 554, L49
- Hawley, J.F., Smarr, L.L., & Wilson, J.R. 1984a, *ApJ*, 277, 296
- Hawley, J.F., Smarr, L.L., & Wilson, J.R. 1984b, *ApJS*, 55, 211
- Henriksen, R.N., & Heaton, K.C. 1975, *MNRAS*, 171, 27
- Ichimaru, S. 1977, *ApJ*, 214, 840.
- Igumenshchev, I.V., & Abramowicz, M.A. 1999, *MNRAS*, 303, 309
- Igumenshchev, I.V. & Narayan, R. 2002, *ApJ*, 566, 137
- Kryukov, I.A., Pogorelov, N.V., Bisnovatyi-Kogan, G.S., Anzer, U., & Börner, G. 2000, *A&A*, 364, 901
- Lynden-Bell, D. 1978, *PhyS*, 17, 185
- Loewenstein, M., Mushotzky, R.F., Angelini, L., Arnaud, K.A., & Quataert, E. 2001, *ApJ*, 555, L21
- Machida, M., Matsumoto, R., & Mineshige, S. 2001, *PASJ*, 53, L1
- Melia, F. 1992, *ApJ*, 387, L25
- Melia, F. 1994, *ApJ*, 426, 577
- Mészáros, P. 1975, *A&A*, 44, 59
- Molteni, D., Lanzafame, G., & Chakrabarti, S. 1994, *ApJ*, 425, 161
- Narayan, R., Igumenshchev, I.V., & Abramowicz, M.A. 2000, *ApJ*, 539, 798
- Narayan, R., Quataert E., Igumenshchev, I.V., & Abramowicz, M.A. 2002, *ApJ*, submitted (astro-ph/0203026)
- Narayan, R., & Yi, I. 1994, *ApJ*, 428, L13
- Narayan, R., & Yi, I. 1995, *ApJ*, 444, 231
- Ostriker, J.P., McCray, R., Weaver, R., & Yahil, A. 1976, *ApJ*, 208, L61
- Paczynski, B., & Wiita, J. 1980, *A&A*, 88, 23

- Quataert, E., & Gruzinov A. 2000, ApJ, 545, 842
- Quataert, E., & Narayan R. 1999, ApJ, 520, 298
- Rees, M.J., Begelman, M.C., Blandford, R.D., & Phinney, E.S. 1982, Nature, 295, 17
- Ruffert, M. 1994, ApJ, 427, 342
- Ryu, D., Brown, G.L, Ostriker, J.P., & Loeb, A. 1995, ApJ, 452, 364
- Shakura, N.I., & Sunyaev, R.A. 1973, A&A, 24, 337
- Shapiro, S.L. 1973, ApJ, 180, 531
- Sparke, L.S. 1982, ApJ, 254, 456
- Sparke, L.S., & Shu, F.H. 1980, ApJ, 241, L65
- Stone, J.M., & Norman, M.L. 1992, ApJS, 80, 753
- Stone, J.M., & Pringle, J.E. 2001, MNRAS, 322, 461
- Stone, J.M., Pringle, J.E., & Begelman, M.C. 1999, MNRAS, 310, 1002
- Toropin, Y.M., Toropina, O.D., Savelyev, V.V., Romanova, M.M., Chechetkin, V.M.,  
& Lovelace, R.V.E. 1999, ApJ, 517, 906

Fig. 1. A sequence of specific angular momentum contours (top) and velocity fields (bottom) from run B04f1a at times 0.03, 0.06, 4.56, and 9.27. The specific angular momentum is in units of  $2R_Sc$ . The minimum of  $l$  (contour closest to the rotational  $z$ -axis) is 0.3 and the contours levels are equally spaced at intervals of  $\Delta l = 0.3$ . Note that the maximum of  $l$  is 3.6 at the beginning of the simulation and 3.3 at the end of the simulation, indicating that lower angular momentum material is displacing higher angular momentum material in the torus. Only the  $l = 0.9$  contour is labeled to show the boundary between the flow that does and does not accrete. We suppressed the velocity in the innermost part of the flow to better show the flow pattern at large radii.

Fig. 2. The specific angular momentum contours and velocity field at the end of run B04f1a. This figure is an enlargement of the rightmost panels from Figure 1. Note that at small radii the nonaccreting flow, the torus, is of nearly constant specific angular momentum. The “figure-8” contour on both panels marks the radial sonic surface (the location where  $M_r = v_r/c_s = 1$ ).

Fig. 3. Quantities at the inner boundary in model B04f1a at  $t_f = 9.27$ . The solid and dashed lines on the top panel show the radial and latitudinal Mach numbers, respectively. The specific angular momentum (middle panel) is in units of  $2R_Sc$  while the mass flux density (bottom panel) is in units of the Bondi mass flux density [i.e.,  $-(\rho v_r)_B \equiv \dot{M}_B/(4\pi r_i^2)$ ].

Fig. 4. Quantities on the sonic surface in model B04f1a at  $t_f = 9.27$ . The top panel shows the sonic radius as a function of the latitude in units of  $R_B$ . The second panel from the top shows  $l$  in units of  $2R_Sc$  (solid line) and the latitudinal Mach number (dashed line). The second panel from the bottom shows the mass flux density in units of the Bondi mass flux density at the radial sonic point. [i.e.,  $-(\rho v_r)_B \equiv \dot{M}_B/(4\pi R_B^2 x_s^2)$ ]. The bottom panel shows a measure of the deviation from radial flow,  $\Delta\theta$ , as defined in the text.

Fig. 5. The time evolution of the mass accretion rate in units of the Bondi rate, for model B04f1a.

Fig. 6. The specific angular momentum contours at the end of run B01f1a. The right-hand panel is an enlargement of the left-hand panel. The “figure-8” contour on the right-hand panel marks the the radial sonic surface (the location where  $M_r = 1$ ). The spacing of the  $l$  contours is as in Figure 1. Note that runs B04f1a (Fig. 1) and B01f1a have different  $l$  distributions at large radii yet at small radii the flows in both runs are qualitatively similar (compare figure 2 and the right-hand panel here).

Fig. 7. The mass accretion rate as a function of  $\theta_o$ . The angle  $\theta_o$  is the polar angle at which  $l = 2R_Sc$  at the outer boundary. The solid line represents results for all of our

Table 1: Summary of parameter survey.

Run*	Resolution	$R'_S$	$R'_C$	$l_0$	$\theta_o$	$f(\theta)$	$t_f$	$l_a^{max}$	$\dot{M}_a/\dot{M}_B$	Comments
A02f1a	100	$10^{-2}$	$2 \times 10^{-1}$	1.6	$68^\circ$	$1 -  \cos \theta $	35	0.80	0.57	
A03f1a	100	$10^{-2}$	$5 \times 10^{-1}$	2.5	$53^\circ$	$1 -  \cos \theta $	36	0.80	0.40	
A04f1a	100	$10^{-2}$	$1 \times 10^0$	3.5	$44^\circ$	$1 -  \cos \theta $	12	0.81	0.50	
A08f1a	100	$10^{-2}$	$1 \times 10^2$	35.3	$14^\circ$	$1 -  \cos \theta $	36	0.87	0.08	
A03f1b	140	$10^{-2}$	$5 \times 10^{-1}$	2.5	$53^\circ$	$1 -  \cos \theta $	441	0.40	0.97	$r_o = 12R_B$
A07f2a	100	$10^{-2}$	$5 \times 10^{-1}$	2.5	$18^\circ$	$1 - \cos^{10} \theta$	31	0.82	0.18	
B01f1a	140	$10^{-3}$	$8 \times 10^{-3}$	1	$90^\circ$	$1 -  \cos \theta $	3.5	0.87	0.30	
B03f1a	140	$10^{-3}$	$5 \times 10^{-2}$	2.5	$53^\circ$	$1 -  \cos \theta $	5.9	0.87	0.30	
B04f1a	140	$10^{-3}$	$1 \times 10^{-1}$	3.5	$44^\circ$	$1 -  \cos \theta $	9.3	0.86	0.30	
B05f1a	140	$10^{-3}$	$5 \times 10^{-1}$	7.9	$29^\circ$	$1 -  \cos \theta $	4.4	0.87	0.24	
B06f1a	140	$10^{-3}$	$1 \times 10^0$	11.2	$24^\circ$	$1 -  \cos \theta $	4.3	0.87	0.22	
B04f1b	180	$10^{-3}$	$1 \times 10^{-1}$	3.5	$44^\circ$	$1 -  \cos \theta $	8.2	0.89	0.30	$r_o = 12R_B$
B08f3a	140	$10^{-3}$	$8 \times 10^{-3}$	1	$8.1^\circ$	step function	6.7	0.88	0.05	
B09f3a	140	$10^{-3}$	$8 \times 10^{-3}$	1	$6.3^\circ$	step function	8.0	0.88	0.04	
B10f3a	140	$10^{-3}$	$8 \times 10^{-3}$	1	$4.5^\circ$	step function	6.7	0.88	0.03	
B08f2a	140	$10^{-3}$	$1 \times 10^{-1}$	3.5	$8.1^\circ$	$1 - \cos^{10} \theta$	6.7	0.88	0.11	
C04f1a	160	$10^{-3.5}$	$3.1 \times 10^{-2}$	3.5	$44^\circ$	$1 -  \cos \theta $	3.6	0.8	0.20	
C08f2a	160	$10^{-3.5}$	$3.1 \times 10^{-2}$	3.5	$8.1^\circ$	$1 - \cos^{10} \theta$	2.7	0.8	0.09	

\* We use the following convention to label our runs: the first character in the name refers to  $R'_S$ , (i.e., A, B, and C are for  $R'_S = 10^{-2}, 10^{-3}$ , and  $10^{-3.5}$ , respectively). The second and third characters refer to  $\theta_o$  (i.e., 01, 02, 03, 04, 05, 06, 07, 08, 09 and, 10 are for  $\theta_o = 90^\circ, 68^\circ, 53^\circ, 44^\circ, 29^\circ, 24^\circ, 18^\circ, 14^\circ, 8.1^\circ, 6.3^\circ$ , and  $4.5^\circ$ , respectively), the fourth and fifth characters refer to the angular distribution of  $l$  (i.e.,  $f1, f2$ , and  $f3$  are for  $1 - |\cos \theta|, 1 - \cos^{10} \theta$ , and the step function (see eq. 25), respectively), and finally the sixth character refers to the outer radius of the computational domain (i.e., a and b stands for  $r_o = 1.2 R_B$  and  $12 R_B$ , respectively).

model with  $R_S/R_B = 10^{-3}$ , regardless of the angular distribution of  $l$  and regardless of  $l_0$  (see Table 1). The dashed line represent the theoretical prediction that  $\dot{M}_a$  scale with the solid angle within which  $l < 2R_{SC}$  at  $R_B$ . The mass accretion rate is in units of the corresponding Bondi rate.

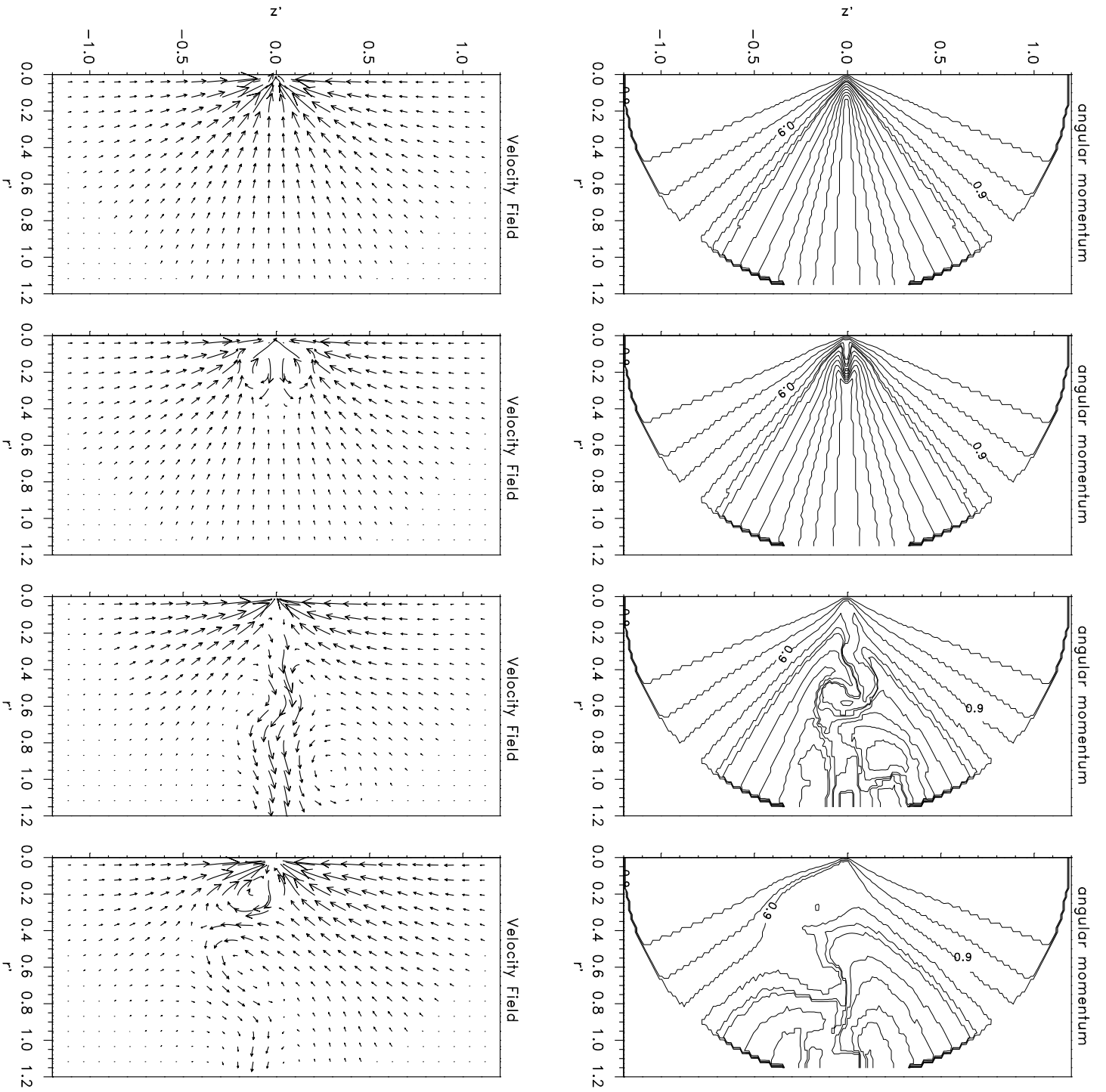


Fig. 1.—

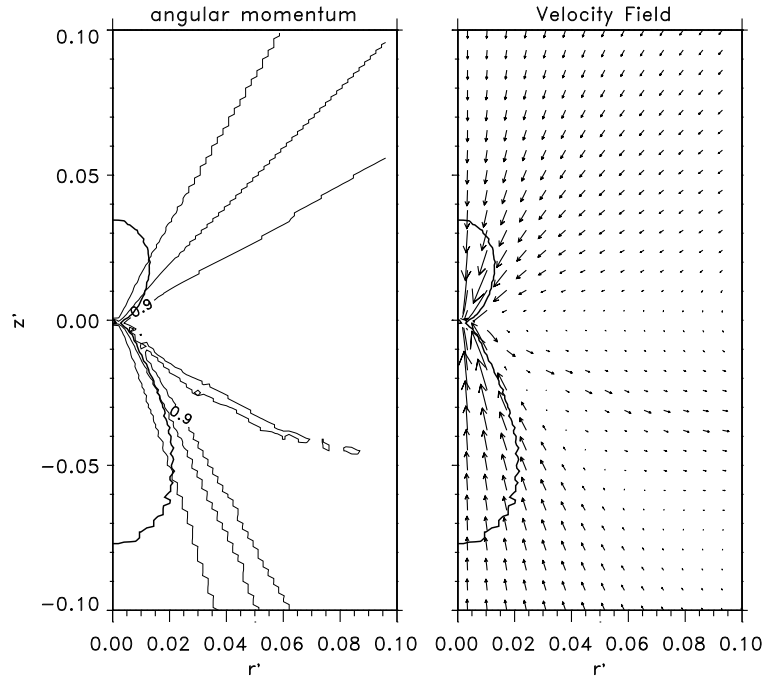


Fig. 2.—

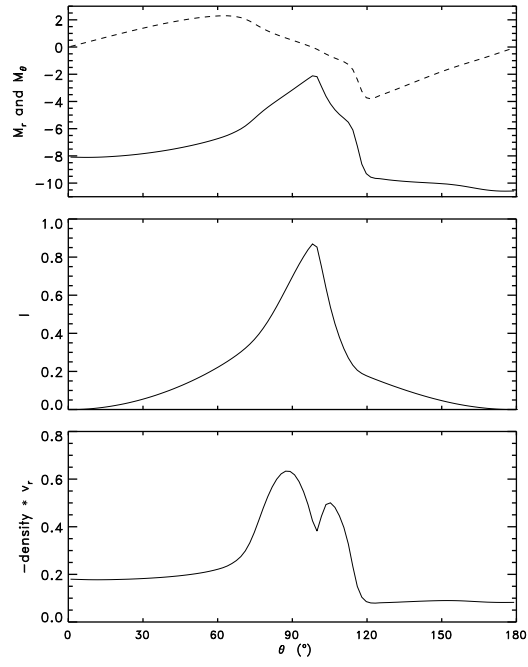


Fig. 3.—



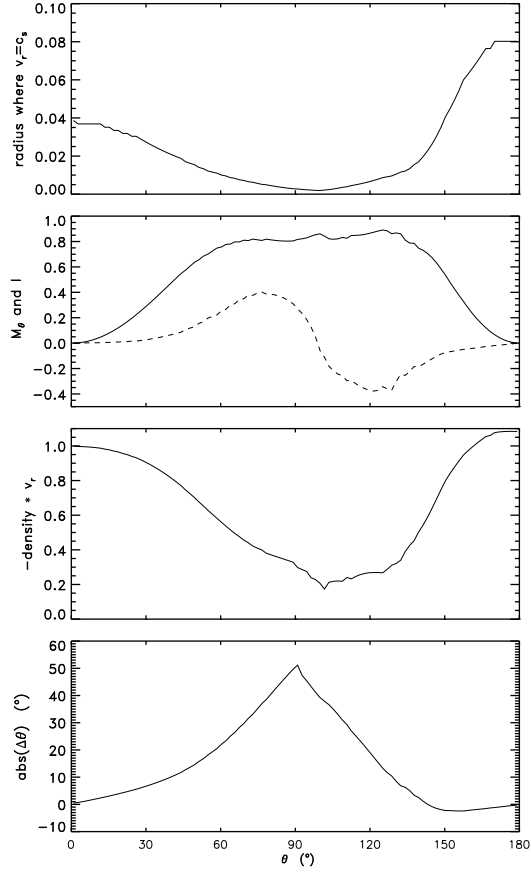


Fig. 4.—

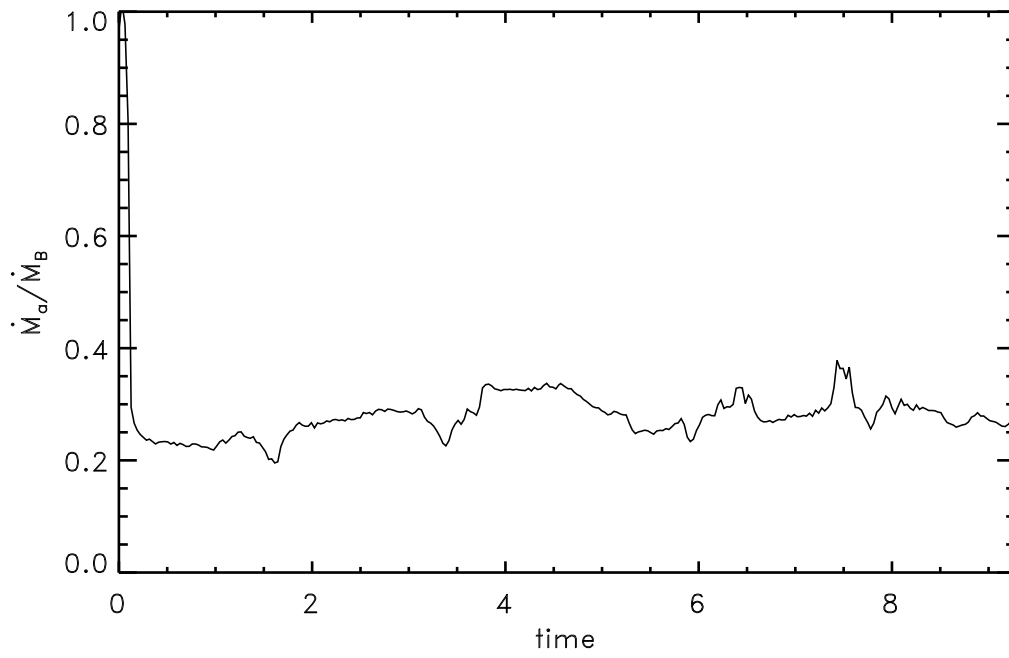


Fig. 5.—

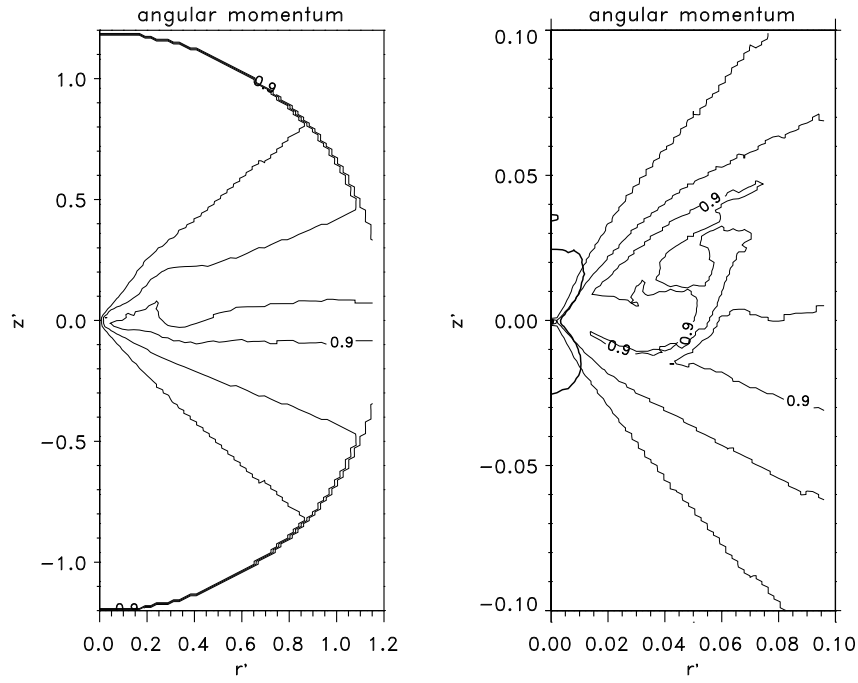


Fig. 6.—

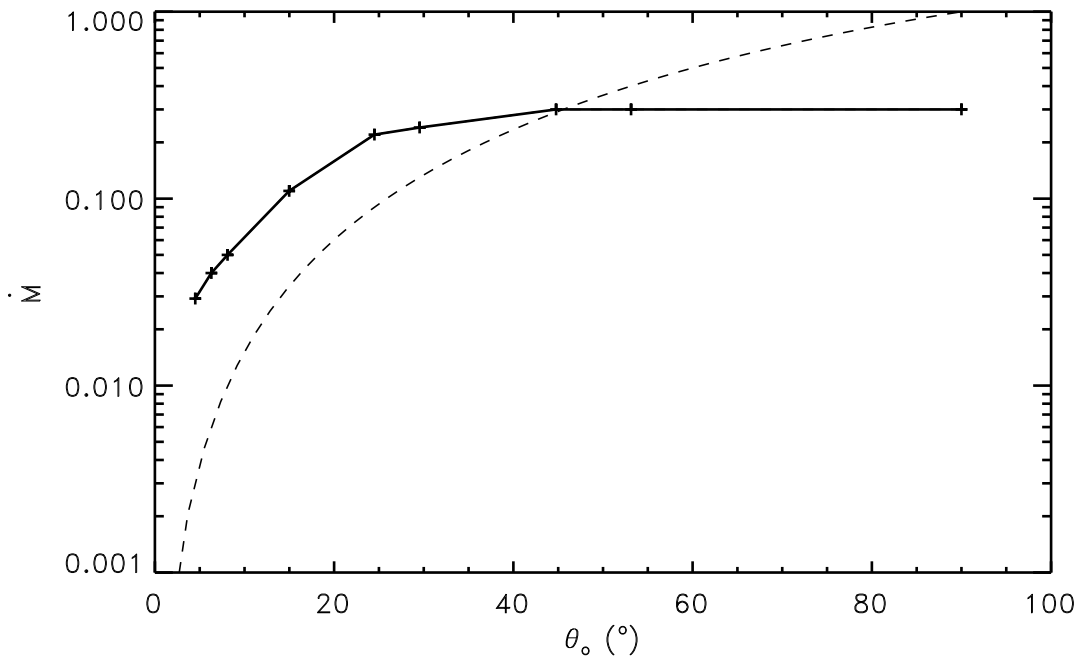


Fig. 7.—